https://doi.org/10.5194/egusphere-2025-637
Preprint. Discussion started: 4 March 2025

Rockwall permafrost dynamics evidenced by Automated Electrical Resistivity Tomography at Aiguille du Midi (3842 m a.s.l., French Alps)

Feras Abdulsamad[1], Josué Bock[1], Florence Magnin[1], Emmanuel Malet[1], André Revil[1], Matan Ben-Asher[1], Jessy Richard[1, 2], Pierre-Allain Duvillard[2], Marios Karaoulis[3], Thomas Condom[4], Ludovic Ravanel[1] and Philip Deline[1]

1. EDYTEM, CNRS - Université Savoie Mont-Blanc, 73370 Le Bourget du Lac, France
2. Naga Geophysics, 229 rue Joseph Fontanet 73000 Chambéry, France
3. School of Geology, Geophysics Department, Aristotle University of Thessaloniki, Thessaloniki, Greece
4. Univ. Grenoble Alpes, IRD, CNRS, INRAE, Grenoble-INP, IGE, 38000 Grenoble, France

Corresponding author: Abdulsamad Feras (feras.abdul-samad@univ-smb.fr)

Emails: feras.abdul-samad@univ-smb.fr; andre.revil@univ-smb.fr; ludovic.ravanel@univ-smb.fr; florence.magnin@univ-smb.fr; mkaraoulis@geo.auth.gr; matan.ben-asher@univ-smb.fr; pierre-allain.duvillard@naga-geophysics.com; josue.bock@laposte.net; emmanuel.malet@univ-savoie.fr; jessy.richard@naga-geophysics.com; thomas.condom@ird.fr; philip.deline@univ-smb.fr

Keywords: Rockwall permafrost dynamics; Active layer thickness; Electrical resistivity tomography; Temperature measurements.

https://doi.org/10.5194/egusphere-2025-637
Preprint. Discussion started: 4 March 2025

Abstract. Permafrost warming significantly affects the stability of rockwalls in high altitude regions. Subsurface monitoring of permafrost is essential to assess the resulting potential geohazards. This study investigates permafrost dynamics at Aiguille du Midi (3842 m a.s.l., French Alps) using an Automated-Electrical Resistivity Tomography (A-ERT) approach, conducted over a period of four years (2020-2023). A total of three geophysical profiles have been installed on three sides of the Aiguille du Midi. An autonomous acquisition system for permanent resistivity monitoring and remote data acquisition is implemented. A time-lapse inversion technique is employed to get time lapse variations of the electrical resistivity of Aiguille du Midi at different time scales. In addition to the field measurements, laboratory measurements of electrical resistivity are conducted on one water-saturated granite sample in both unfrozen and frozen conditions to evaluate the temperature-dependency of resistivity. Temperature information about the thermal state of permafrost is available from three shallow boreholes drilled in 2009, used to validate our interpretation. A-ERT showed significant variations in the active layer thickness across different rock faces, along with a slight decrease in the resistivity of permafrost, indicating its warming over time. Our findings indicate that the temperature dependence of resistivity in field conditions (open system) is slightly less pronounced than in controlled laboratory experiments (closed system). Using a petrophysical model connecting temperature to resistivity, the temperature distribution within the frozen zone can be estimated from the resistivity measurements (during summer and autumn) with an accuracy of ~±1 °C. This research underscores the efficacy of ERT as a promising, non-invasive tool for monitoring permafrost dynamics in Alpine environments. It highlights the need for further methodological refinement to better resolve subsurface properties, potentially using induced polarization data.

https://doi.org/10.5194/egusphere-2025-637
Preprint. Discussion started: 4 March 2025

1. Introduction

Climate change accelerates the degradation of the cryosphere in high-mountains areas worldwide (Etzelmüller et al., 2020). Over the last decade, there has been a continuous increase in rockfall events, particularly those affecting permafrost in the European Alps (Cathala et al., 2024; Jacquemart et al., 2024; Ravanel et al., 2017). Infrastructures located in high altitude are increasingly affected by these events (Offer et al., 2025; Duvillard et al., 2021, 2018). Permafrost degradation/warming of the rock mass can also locally be accelerated by heat advection through water infiltration in fractures causing the erosion of the ice-infill (Hauck and Hilbich, 2024). As a result, a loss of bonding between rock and ice may occur, changing in turn the mechanical properties of such assemblage (Krautblatter et al., 2013). Understanding the thermohydrological dynamics of steep Alpine rock faces is essential for assessing potential geohazards associated with permafrost degradation.

Rockwall temperatures can be directly determined and monitored using temperature sensors installed at the rock surface or in boreholes (*e.g.*, Magnin et al., 2024). While borehole temperature monitoring is still the only direct method to detect the occurrence of permafrost, it provides only local information. That said, permafrost dynamic can be controlled by various processes such as water flows in fractures, that are not fully captured by point-scale temperature measurements (Hauck and Hilbich, 2024). In addition, boreholes in rockwall at high altitude are logistically difficult to realize. They are also expensive and invasive.

Geophysical measurements provide high spatial coverage with respect to boreholes. Various non- or minimally intrusive methods have been applied to evaluate permafrost, including Refraction Seismic Tomography (RST) (*e.g.*, Steiner et al., 2019; Draebing 2016), Ground Penetrating Radar (GPR) (Campbell et al., 2018), Electrical Resistivity Tomography (ERT) (*e.g.*, Mollaret et al., 2020; Krautblatter and Hauck 2007) and Induced Polarization (IP) (Maierhofer et al., 2024; Abdulsamad et al., 2019; Duvillard et al., 2018; Doetsch et al., 2015).

https://doi.org/10.5194/egusphere-2025-637
Preprint. Discussion started: 4 March 2025

Combined geophysical methods can take advantage of the complementary petrophysical and spatial sensitivities of these different methods. For instance, ERT measurement was combined with RST to evaluate ice, air, water, and rock contents (Mewes et al., 2017; Hauck et al., 2011). Recently, joint inversion of ERT and RST could reduce the uncertainties in the evaluation of air, water, ice and rock contents (Pavoni et al., 2023; Steiner et al., 2021; Mollaret et al., 2020; Wagner et al., 2019). IP measurements (providing tomograms of the electrical conductivity and normalized chargeability) have been recently used to assess the distribution of permafrost temperature, relying on laboratory calibration and a petrophysical (physics-based) model connecting resistivity and normalized chargeability with temperature under frozen and unfrozen conditions (see Moser et al., 2025; Duvillard et al., 2021, 2018, and references therein).

In the last few years, ERT has become an increasingly popular tool in permafrost studies (*e.g.*, Herring et al., 2023; Farzamain et al., 2020; Magnin et al., 2015a; Krautblatter et al., 2010). Herring et al. (2023) provide a review of the use of ERT method in permafrost research, detailing both the advantages and limitations of this method in such a context. A significant advantage of using electrical resistivity measurements to assess mountain permafrost is that the freezing and thawing of water filling pores are associated with considerable changes in resistivity (generally between one to three orders of magnitude, see Coperey et al., 2019). Because of this sensitivity, electrical resistivity tomograms can be used to assess of the presence and distribution of permafrost.

Repeated ERT measurements at specific time intervals using the same survey geometry can be used to track the temporal and spatial evolution of permafrost over time (*e.g.*, Offer et al., 2025). However, rapid changes due to water flux, infiltration or drainage (such as during snowmelt or rainfall) may not be captured by monthly or seasonally repeated measurements (Krautblatter et al., 2010). Alternatively, continuous resistivity measurements, known as Automated-ERT (A-ERT) or ERT monitoring, offer the ability to track the ongoing evolution

https://doi.org/10.5194/egusphere-2025-637
Preprint. Discussion started: 4 March 2025

of permafrost and capture rapid changes in its temperature and ice content (*e.g.*, Scandroglio et al., 2021; Doetsch et al., 2015). A-ERT over period of several years has been recently used to track the degradation of permafrost associated with global warming (Mollaret et al., 2019; Keusching et al., 2017; Doetsch et al., 2015; Hilbich et al., 2008).

Furthermore, the time-lapse inversion of geophysical data derived from fixed monitoring network provides a succession of tomograms showing the changes in subsurface resistivity (see; Karaoulis et al., 2013; Loke, 1999). Results of time-lapse inversion of apparent resistivity data can be directly related to the evolution of permafrost during the yearly cycle or rapid variations caused by water infiltration or drainage during short periods of time.

That said, A-ERT at high altitudes (>3500 m) has not yet been tested for long-term permafrost monitoring. The use of A-ERT under high-altitude conditions presents specific challenges due to extreme climatic conditions and meteorological events. However, it could provide valuable information about the evolution of permafrost.

In this study, we present the results of an A-ERT survey conducted over four years (2020-2023) at Aiguille du Midi (AdM) in the Mont-Blanc massif (French Alps). The objective of this study is to examine permafrost dynamics from infra-seasonal to multiyear timescales. Our goals include: (1) evaluating the potential of A-ERT to characterize permafrost dynamics in steep alpine rockwalls; (2) assessing the accuracy of temperature derived from resistivity measurements; and (3) studying the hydrogeological system, including water infiltration and drainage in fractures, along with their thermal impacts. For this objective, a total of three 155-m-long profiles were deployed downwards from the summit in three directions: North-West (NW), South (S) and East (E). Each profile consists of 32 electrodes spaced at 5 m. In addition to field data, laboratory resistivity measurements were conducted on granite core sample, in both unfrozen and frozen conditions. Furthermore, temperature which was continuously

https://doi.org/10.5194/egusphere-2025-637
Preprint. Discussion started: 4 March 2025

monitored in three shallow boreholes, one of them is located along the ERT profile, is used to validate our interpretation of the geophysical measurements.

2. Study site

We investigate the iconic Aiguille du Midi (3842 m a.s.l.), which is the highest and most western summit of the Aiguilles de Chamonix. It is located on the north-west flank of the Mont-Blanc massif (Fig. 1a). It includes three peaks that are all connected by human-made bridges and galleries. In average, AdM is visited in summer by around 5000 visitors a day transported from the city of Chamonix by cable-cars. The appearance of the summit of AdM has been greatly affected by the construction and developments carried out since the 1950s (see Fig. 1). Our study focuses on the central peak, which is the highest among the three, and which hosts the cable-car station connecting AdM to Pointe Helbronner with the *Panoramic Mont-Blanc* cable car. The lithology in the study area is dominated by massive granite with a very low porosity (~ 0.01, Magnin et al., 2015a). The highest parts (3740 to 3840 m a.s.l.) of the peak tend to be steep, contain few large fractures, and, in places, are characterized by vertical foliation bands and small cracks (Magnin et al., 2015b). Figure 2 shows the mean monthly and annual air temperature at AdM during the study period. The year 2021 was the coolest year (yearly averages: -5.8 °C, -6.9 °C, -5.3 °C, and -5.7 °C from 2020 to 2023, respectively).

In order to evaluate the thermal state and the distribution of permafrost at AdM, three boreholes have been drilled in 2009. They are labeled BH-NW on the NW face, BH-S on the South face and BH-E on the East face. Each borehole is 10-m-deep and 66 mm in diameter, and were drilled normal to the topography (their position is shown in Fig. 1). Each borehole is equipped with 15-thermistor strings calibrated in an ice-water bath and then placed at different depths in the borehole. In the past few years, the temperature of the permafrost core is highly variable from one face to another, with temperature of about −4 °C at 10 m depth of the NW face to −1 °C at the same depth in the sun-exposed (S face) (Magnin et al., 2024). Those

https://doi.org/10.5194/egusphere-2025-637
Preprint. Discussion started: 4 March 2025

temperature differences imply strong temperature gradient within the rock mass. In the same way, the Active Layer Thickness (ALT, *i.e.*, the maximum seasonal thaw layer that derived from temperature measurements) is also highly variable: it is observed to be around 1.6 to 2.7 m at the end of summer on the NW side, while it reaches 6.8 m on the S side. Below this depth, permafrost is present all along the year (see details in Magnin et al., 2024).

BH-NW is located along an electrical resistivity profile (NW profile) and is positioned between electrodes 8 and 9 (counted from the bottom) of the NW profile (see Fig. 1c). The temperature measured in this borehole is used to assess the accuracy of the temperature derived from ERT results using the petrophysical model presented in the next section.

https://doi.org/10.5194/egusphere-2025-637
Preprint. Discussion started: 4 March 2025

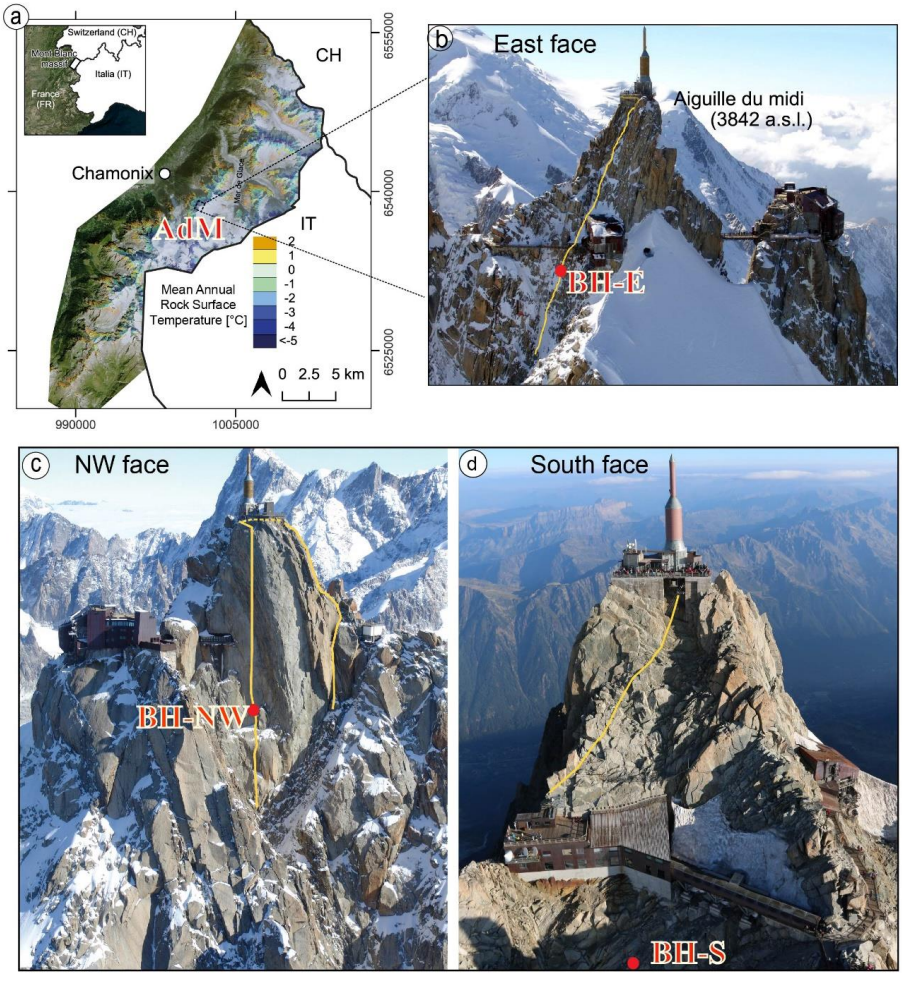

Figure 1. Study site location and geophysical survey setting. The yellow lines indicate the approximate positions of electrical resistivity profiles on each side (NW, E and S profiles). The red dots denote the borehole locations. (a) Location of the study site (Aiguille du Midi (AdM)), in the Mont Blanc massif (here, the French side) largely affected by the permafrost (from, Magnin et al. (2015b)). (b) The electrical resistivity profile and borehole locations at the East face. (c) The electrical resistivity profile and borehole locations at the North-West face. (d) The electrical resistivity profile and borehole locations at the South face.

https://doi.org/10.5194/egusphere-2025-637
Preprint. Discussion started: 4 March 2025

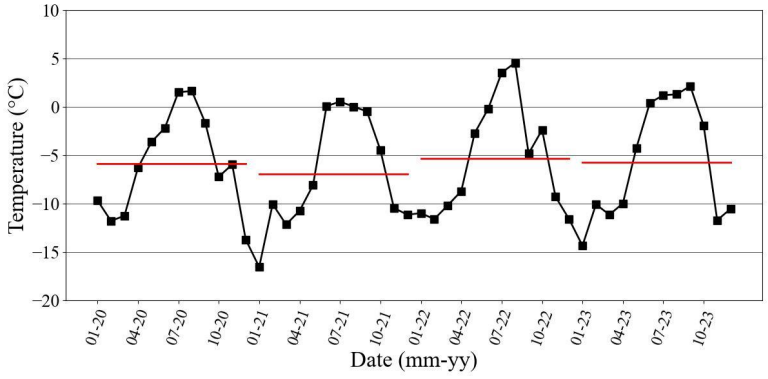

Figure 2. Monthly average air temperature (°C) at AdM during the survey period (Data from the meteorological station of Institute of Environmental Geosciences at the Aiguille du Midi). Horizontal bars show the annual average air temperature.

3. Electrical conductivity - temperature relationship

The electrical conductivity of a rock represents its ability to conduct an electrical current under the application of an imposed electrical field. The electrical conductivity (inverse of the electrical resistivity) of a rock depends on its porosity ϕ (dimensionless), water content θ (dimensionless), pore water conductivity, Cation Exchange Capacity (CEC), and rock temperature T (in °C) (*e.g.*, Revil et al., 1998).

Above the freezing point (typically, but not necessary, around 0°C), electrical conductivity ($\sigma(T)$ in S m^{-1}) increases linearly with temperature according to Revil et al. (1998):

$$\sigma(T) = \sigma(T_0)\left[1+\alpha_T(T-T_0)\right], \qquad (1)$$

where α_T = 0.021±0.02 °C^{-1}, T_0 = 25°C denotes the reference temperature, and $\sigma(T_0)$ denotes the conductivity of the rock at the reference temperature.

In contrast, under freezing conditions, temperature variations have a significant influence on electrical conductivity because of the occurrence of an insulating phase (*i.e.*, ice formation) in the pore space and despite the increase in the salinity of the pore water with

https://doi.org/10.5194/egusphere-2025-637
Preprint. Discussion started: 4 March 2025

temperature decrease. This temperature dependence of electrical conductivity can be modeled as follows (see details in Duvillard et al., 2021; 2018; Coperey et al., 2019):

$$\sigma(T) \approx \left[(\phi - \theta_r) \exp\left(-\frac{T - T_F}{T_C} \right) + \theta_r \right] \frac{\sigma(T_0)}{\phi} \left[1 + \alpha_T (T - T_0) \right], \quad (2)$$

Where θ_r (dimensionless) denotes the residual water content when T<<T_F, T_F denotes the liquidus or freezing point/temperature, T_C denotes a characteristic temperature controlling the transition between the unfrozen state and the frozen state, and $\phi - \theta_r$ denotes the maximum volumetric ice content at low temperatures. Equation (2) provides the opportunity to convert electrical conductivity or electrical resistivity tomogram measured in the field to a temperature distribution (*e.g.*, Duvillard et al., 2021).

4. Methods

4.1 Laboratory measurements

To evaluate the parameters (*e.g.*, T_C, θ_r) in the petrophysical model discussed above (Section 3), and to calibrate our field measurements, we conducted an electrical conductivity experiment on a granite rock sample collected from an outcrop on the site. The granite (cubic) core sample was dried during 24 h at around 100°C, then saturated under vacuum with degassed water. The water conductivity was measured to be 0.016 S m^{-1} (representative of water from melted snow in the field) at equilibrium at T = 25˚C. The sample was left in the solution for several weeks to reach chemical equilibrium before performing the laboratory measurements.

The sample was installed in a heat-resistant insulating bag immersed in a thermostat bath (KISS K6 from Huber; dimensions: 210×400×546 mm; bath volume: 4.5 L). The temperature of the bath was controlled with a precision of 0.1 °C. Glycol was used as the heat carrying fluid. The complex conductivity spectra were obtained over the temperature range of

https://doi.org/10.5194/egusphere-2025-637
Preprint. Discussion started: 4 March 2025

+10 to −10 °C, using a high-precision impedance-meter ZEL-SIP04-V02 (Zimmermann et al., 2008). The resistivity measurements reported here are at a frequency of 1 Hz.

For comparison, Figure 3 presents the measurement results for the granite sample from the study site (labeled Sample AdM) alongside measurements from another granite sample (Sample Cosmiques) collected at the lower Cosmiques ridge (Mont-Blanc massif, 3613 m a.s.l.) as reported by Duvillard et al. (2021). The experimental datasets are presented along with data fits, using Equations 1 for temperatures above the freezing point, and Equation 2 for temperatures below the freezing point. We see that the model proposed in Section 3 is able to fit the data above and below the freezing temperature, providing a proxy for connecting electrical conductivity or electrical resistivity to temperature. Furthermore, the Sample AdM was characterized by a very low porosity $\phi = 0.014$.

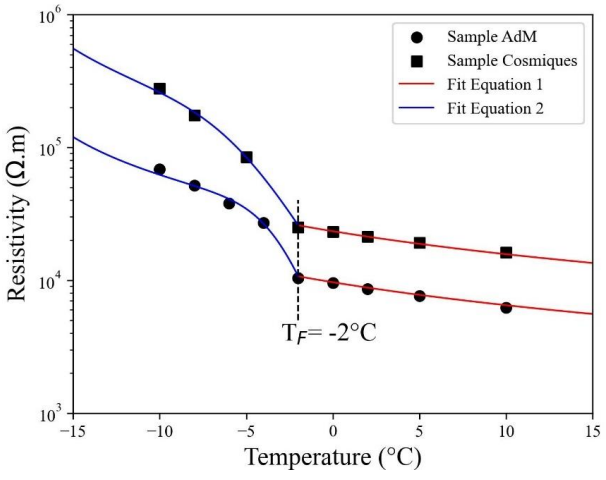

Figure 3. Resistivity-temperature relationship from laboratory measurements on two granite samples from (1) the study site (Sample AdM), and (2) from the Cosmiques ridge, Mont-Blanc massif, West (3613 m a.s.l.) (Sample labeled Cosmiques). T_F denotes the freezing temperature. The solid lines correspond to the fits using the Equation 1 (red lines) and Equation 2 (blue lines), in unfrozen and frozen conditions, respectively. The parameters of the model in Equation 2 are (T_C=-1.3 °C, θ_r=0.004, $\sigma(T_0)$ = 2.3×10^{-4} S m^{-1}) for Sample AdM, and (T_C= -2.17 °C, θ_r = 0.004, $\sigma(T_0)$ = 9.5×10^{-5} S m^{-1}) for Sample Cosmiques.

https://doi.org/10.5194/egusphere-2025-637
Preprint. Discussion started: 4 March 2025

4.2 ERT Data acquisition

A-ERT has been conducted over a four-years period (06/2020 - 12/2023). A total of three cables, each with 32 take-outs spaced 5 m (for a profile length of 155 m), were installed. The three cables were deployed downwards from the summit in three directions: North-West (NW), East (E) and South (S). The S profile starts at the South side and pass to the North-West side around mid-distance (see Fig. 1d). The installation of cables was gradual (over a year) starting from NW side (installed in June 2020), then on the South side (installed in July and August 2020), and finally on the East side (installation finished in March 2021 because of snowpack in 2020 at this side). In order to ensure good electrical contact between electrodes and rock mass, stainless steel (A4/316) climbing bolts (Fischer 10×126 mm) poured in salty bentonite were used and placed firmly in holes drilled in the rock. A specially designed jumper was used to attach each take-out to the bolt to ensure maximum contact. The electrodes remained embedded in the rock wall for all subsequent resistivity measurements. The resistivity cables were attached to anchors to minimize damage from rockfall and snow pressure.

A LS2-Terrameter (ABEM) was used for the data acquisition with internal impedance of 20 MΩ. The ERT device and control system for monitoring were deployed inside the summit station with network access, power connection, and overvoltage protection. Data acquisition was fully automated and remotely controlled. Finally, the position of every electrode was measured using a differential GPS when the signal is available and a theodolite in steep areas. The measurements themselves were carried out using a Wenner configuration (voltage electrodes in between the current electrodes), which leads to a high signal-to-noise ratio and is largely applied in mountain permafrost environments (Mollaret et al., 2020; Krautblatter and Hauck, 2007; Dahlin and Zhou, 2004).

https://doi.org/10.5194/egusphere-2025-637
Preprint. Discussion started: 4 March 2025

The first measurements were performed in June 2020. Then the continuous measurements started in late September 2021 after developing an automated system of acquisition. In the period June 2020 and September 2021, ERT measurements were repeated occasionally. A Contact Resistance (CR) test was performed before each series of measurements. A high contact resistance in the rock wall (>100 kΩ) was encountered throughout the entire survey period, which posed a challenge to the continuity of data acquisition. Figure 4 shows the evolution of contact resistance for each electrode over time for the NW and S profiles. We notice that CR varies between a few kΩ and 10 000 kΩ (see Fig. 4). However, beyond a CR threshold, the ERT measurements lose their accuracy. Electrodes with high CR (>600 kΩ) are excluded automatically by the LS2, leading to gaps in the pseudo-section of apparent resistivity.

The A-ERT ran into numerous software and hardware issues, resulting in unsystematic data gaps. The E face cable was severely damaged by a lightning strike, before being totally destroyed by an uncontrolled rock purge. Additionally, NW and S cables were both damaged by rockfall, leading to significant data gaps (see Fig. 4)., Repairing or replacing the damaged cables was not possible for several reasons (limited access to the cable path because of accumulated snowpack). Datasets were recorded for each profile (NW, S and E profiles) and two long profiles of 64 electrodes (*i.e.*, profile NW+E and profile NW+S).

https://doi.org/10.5194/egusphere-2025-637
Preprint. Discussion started: 4 March 2025

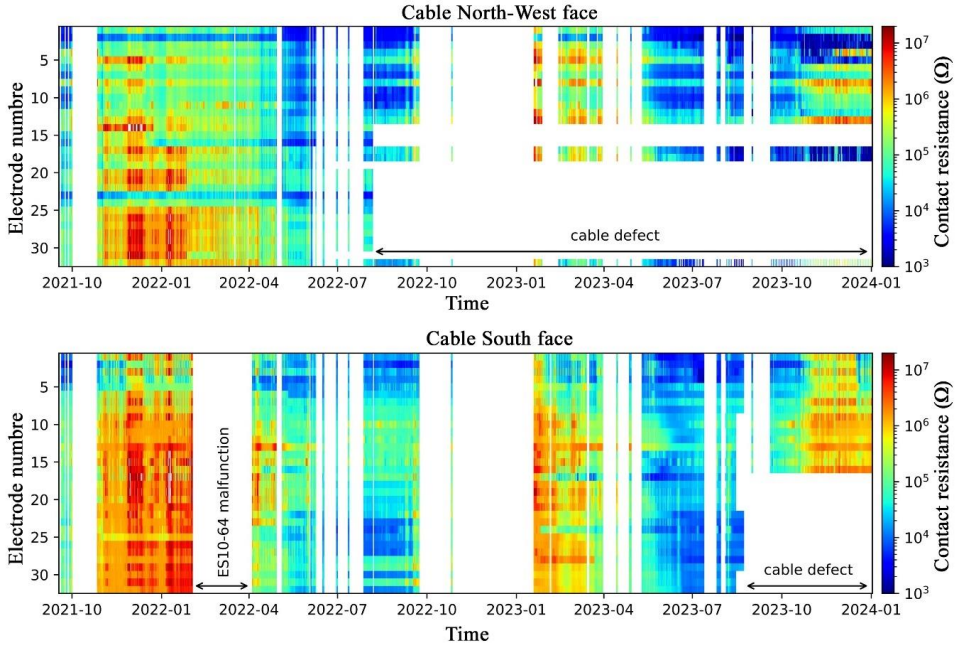

Figure 4. Temporal evolution of contact resistance at the North-West side and South side. Data partly missing are due to cable defects.

4.3. Data processing and inversion

As expected, data from A-ERT are of lower quality than manual measurements where the user can intervene to improve contact resistance after each electrode check (Doetsch et al., 2015; Hilbich et al., 2009). Therefore, the first challenge was evaluating data quality and rejecting poor dataset. The primary criterion was the number of connected electrodes. We tolerated up to four unconnected electrodes (because of high RC) in a pseudo-section depending on their positions, as the contribution of electrodes is not equal in the pseudo-section. The datasets used in this study were selected from overall available data to support the objectives of this study. After selecting valid datasets, outliers within each pseudo-section were removed. Table 1 summarizes the data presented in this study. Most datasets have more than 80 % of the original recorded data points of each pseudo-section.

https://doi.org/10.5194/egusphere-2025-637
Preprint. Discussion started: 4 March 2025

Table 1. summary of data presented in this study. Number of data before filtering is 155 datum points of Wenner configuration. Most of datasets has more than 80% of total number of measurements. Two datasets have more than 40% of lost data because of disconnected electrodes. The Data corresponds to the data of the data acquisition.

Date	N-W Profile		S Profile	
	Number of data after filter	Percentage (%)	Number of data after filter	Percentage (%)
30-06-2020	151	97.5	-	-
26-08-2020	149	96.1	90	58
17-09-2020	151	97.5	90	58
12-04-2021	118	76.1	121	78
09-07-2021	114	73.5	-	-
12-08-2021	149	96.1	140	90.3
17-09-2021	145	93.5	131	84.5
25-09-2021	143	92.2	144	92.9
29-03-2022	121	78	-	-
25-04-2022	141	91	131	84.5
14-05-2022	141	91	147	94.8
24-05-2022	140	90.3	146	94.1
30-06-2022	102	65.8	-	-
30-07-2022	-	-	145	93.5
15-08-2022	-	-	145	93.5
15-09-2022	-	-	144	93
19-03-2023	-	-	138	89
28-04-2023	-	-	143	92.2
25-05-2023	-	-	148	95.5
25-06-2023	-	-	144	92.9
29-07-2023	-	-	140	90.3

Furthermore, existing infrastructure with metal supports and the harsh topography of the site also affect data quality. The topography is characterized by vertical rock walls with an average slope of 78° on the North-West face, which posed some challenges in inversion software.

https://doi.org/10.5194/egusphere-2025-637
Preprint. Discussion started: 4 March 2025

The inversion of the electrical resistivity datasets was performed using the open-source package pyGIMLI (Rücker et al., 2017; Günther et al., 2006). The inversion used a Gauss-Newton minimization algorithm of a cost-function penalizing the roughness of the electrical resistivity distribution on an irregular grid (Günther et al., 2006). In the absence of reciprocal dataset to estimate errors in measurements, we used a linear error model which assumed 5 % relative error. An analysis was conducted to select the regularization parameters that minimize the data misfit of individual inversions of the reference dataset.

5. Results

5.1. Overview of the raw data

Our interpretation began with an analysis of the measured apparent resistivity data (all selected data presented in this study before processing or filtering). This analysis can provide insights into subsurface conditions. Figure 5, shows the variations of the average apparent resistivity (*i.e.*, the average apparent resistivities associated with the same electrode distance (or pseudo-depth) in the pseudo-section), at different electrode distances or different depths of investigation. A difference can be observed between data on the S and NW profiles under unfrozen conditions (Fig. 5a and b). On the North-West face (NW profile) (Fig. 5a), the apparent resistivity is higher at depth (indicating frozen conditions) and lower near the surface (thawing conditions). In contrast, the South face (Fig. 5b) exhibits high values near the surface, related to the fractured area filled with air (resistive material), which increases the medium's resistivity, while lower values are found at greater depths due to close to 0°C conditions depicting warm permafrost (*i.e.*, permafrost with temperature is > -2°C), or increased water saturation. In frozen conditions (Fig. 5c and d), a cooling effect is obvious near the surface on both sides. It is characterized by high apparent resistivity values (~120 kΩm) that decrease with depth.

https://doi.org/10.5194/egusphere-2025-637
Preprint. Discussion started: 4 March 2025

Figure 6 shows the seasonal variation in the apparent resistivity over time of various electrodes quadrupoles (*i.e.*, at varying depths of investigation). Notably, data from the NW profile (a massive rock area) shows moderate variations over time. In contrast, the apparent resistivity variation is more significant at the Southern face (S profile), where a fracture zone may be filled with water, ice, or air throughout the year. Furthermore, the seasonal variation of apparent resistivity is more pronounced for shallow data (correlated with smaller distance between electrodes) on both sides (see further discussion below).

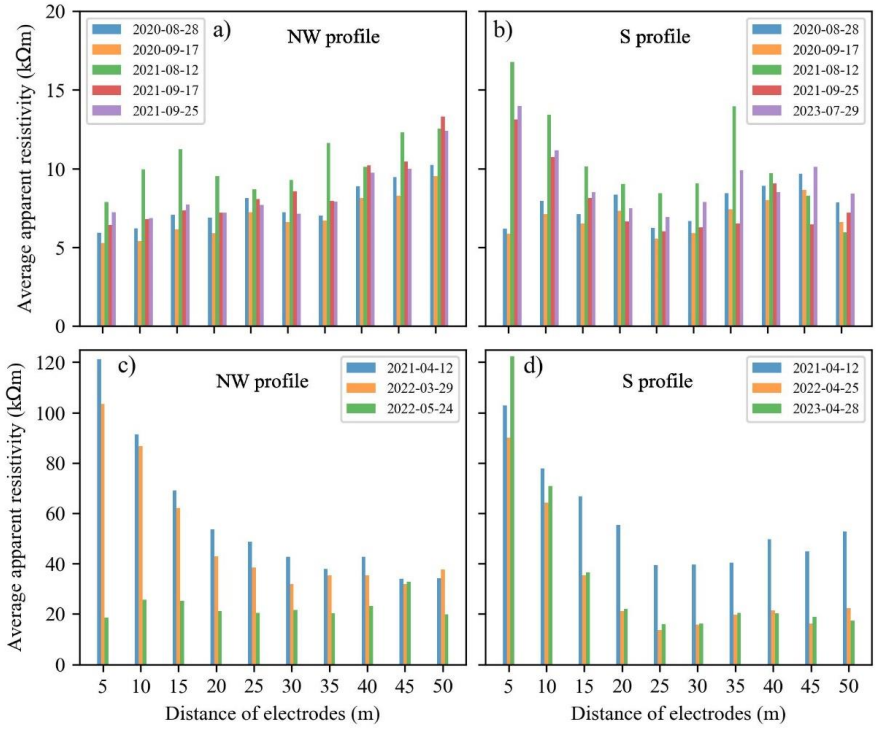

Figure 5. Variations of average apparent resistivity at different electrode distances (*i.e.*, at varying depths of investigation). The upper parts display data collected in summer and autumn (unfrozen condition at surface), and the lower parts show data collected in spring (frozen conditions at surface).

https://doi.org/10.5194/egusphere-2025-637
Preprint. Discussion started: 4 March 2025

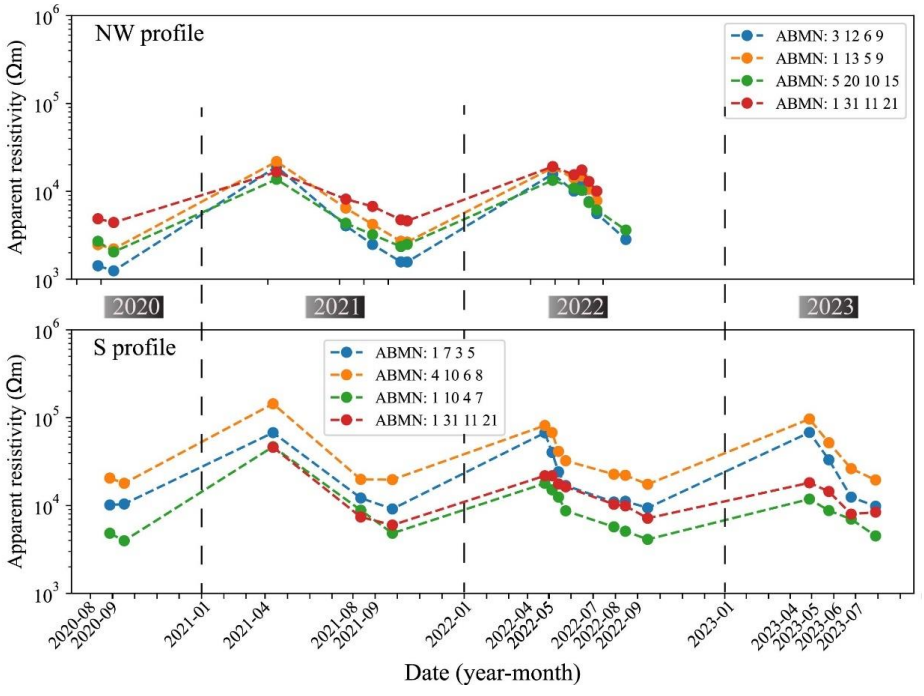

Figure 6. Temporal changes in apparent resistivity for different combinations of quadrupoles (ABMN) reflecting different depths of investigation. The upper section displays data collected from NW profile, while the lower section shows data collected from S profile. Data acquisition on the NW profile stopped at the end of July 2022 after a cable issue.

5.2. Data inversion and interpretation

In order to have an overview of the internal structure of the study site based on the resistivity distribution, we carried out inversions of two long profiles (NW+S and NW+E). Figure 7 shows the electrical resistivity tomogram from late summer 2020 (August 26th, 2020), where acquisition at both North-West and South sides (NW+S) are performed. The tomogram clearly reveals the site's internal structure, with low resistivity areas (warm-colored zones) indicating the relative positions of the infrastructure elements (elevator and galleries on both sides). It also shows the extent of the active layer (moderate resistivity areas), as well as the permafrost evidenced by high resistivity areas (represented in cool-colors). Although the lower

https://doi.org/10.5194/egusphere-2025-637
Preprint. Discussion started: 4 March 2025

part of the tomogram appears similar on both the NW and S sides, which is expected since they lie in rockwalls that are alike regarding slope and aspect (Fig 1c), significant differences are evident in the upper part (*i.e.*, above the gallery level), revealing the contrast between sun-exposed (S side) and shaded face (NW side). For further analysis, the inverted resistivities were extracted from the four locations (P1 to P4) indicated by the red lines in Figure 7 and shown in the inset figure (see Fig. 7). In profile P1, a slight increase in resistivity is observed with depth, rising from 9.5 kΩm to 18 kΩm. Profile P2 exhibits significant variations with depth, characterized by an initial increase followed by a decrease, which can be attributed to the presence of permafrost between the active layer (close to the surface) and the effect of the elevator (at greater depths). Conversely, profile P3 shows higher resistivity near the surface (desaturation effect). The electrical resistivity decreases with depth, likely due to increased water saturation with depth in this area characterized by open fractures. Profile P4 shows a similar trend to profile P1 but exhibits a more pronounced gradient with depth (from 2 kΩm to 27 kΩm). This variation is attributed to heat transfer, particularly in areas close to the sun-exposed face.

https://doi.org/10.5194/egusphere-2025-637
Preprint. Discussion started: 4 March 2025

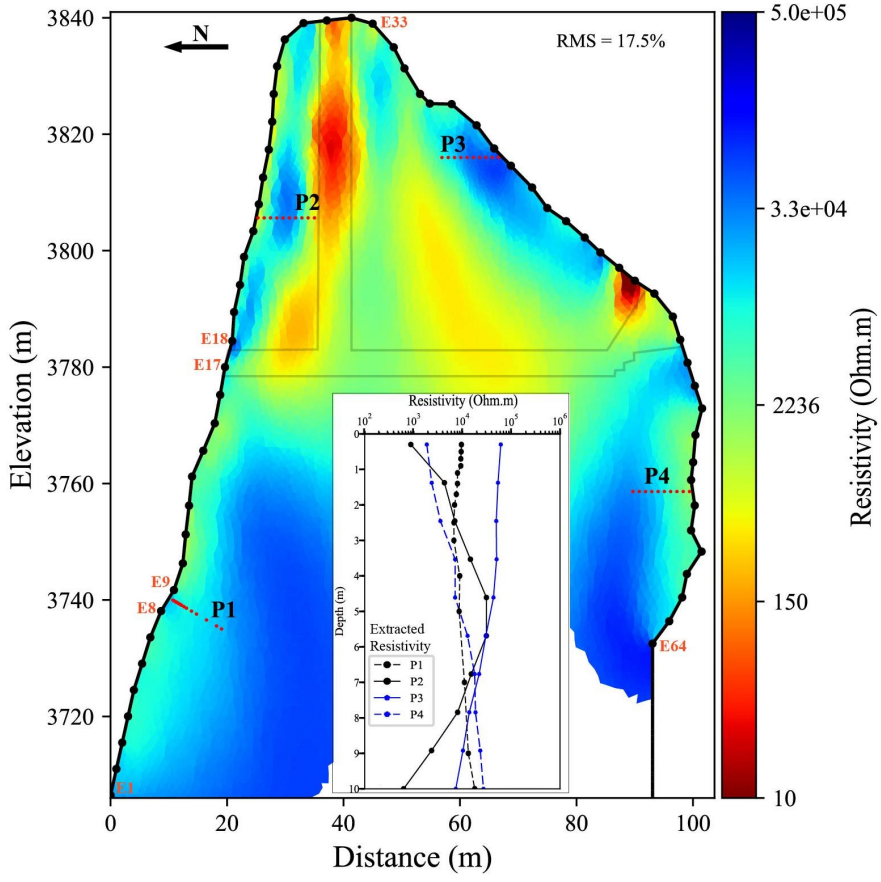

Figure 7. Electrical resistivity tomogram over the NW+S profile measured on August 26, 2020. Grey lines indicate the approximative positions of infrastructure (galleries and elevator). Electrode numbers are shown in red. Red dots (P1 to P4) indicate the positions of extracted resistivity shown in the inset figure. The insert shows the variation of resistivity with depth at the four locations (P1 to P4).

Figure 8 provides an example of the resistivity tomogram for the combined NW and E profiles. This tomogram highlights the changes in resistivity associated with permafrost, active layer, and anthropogenic installation (such as the elevator and gallery). On the Eastern side, the active layer could be observed below a high resistivity layer that likely indicates the dry layer, and higher resistivity at depth that indicates the permafrost. Resistive zones close the surface and round the active layer can be seen, likely resulting from water drainage at the end of the thawing season, creating an unsaturated and air-filled zone surrounded by the active layer where

https://doi.org/10.5194/egusphere-2025-637
Preprint. Discussion started: 4 March 2025

no drainage or weak drainage could be existed. On the other hand, data acquisition on the Eastern side (E profile) encountered numerous challenges related to contact resistance, rockfalls and cable connections, resulting in long gaps and insufficient data for long time analysis or time-lapse inversion. After this overview of the internal structure, a time-lapse inversion of the data of each profile will be presented in the next section.

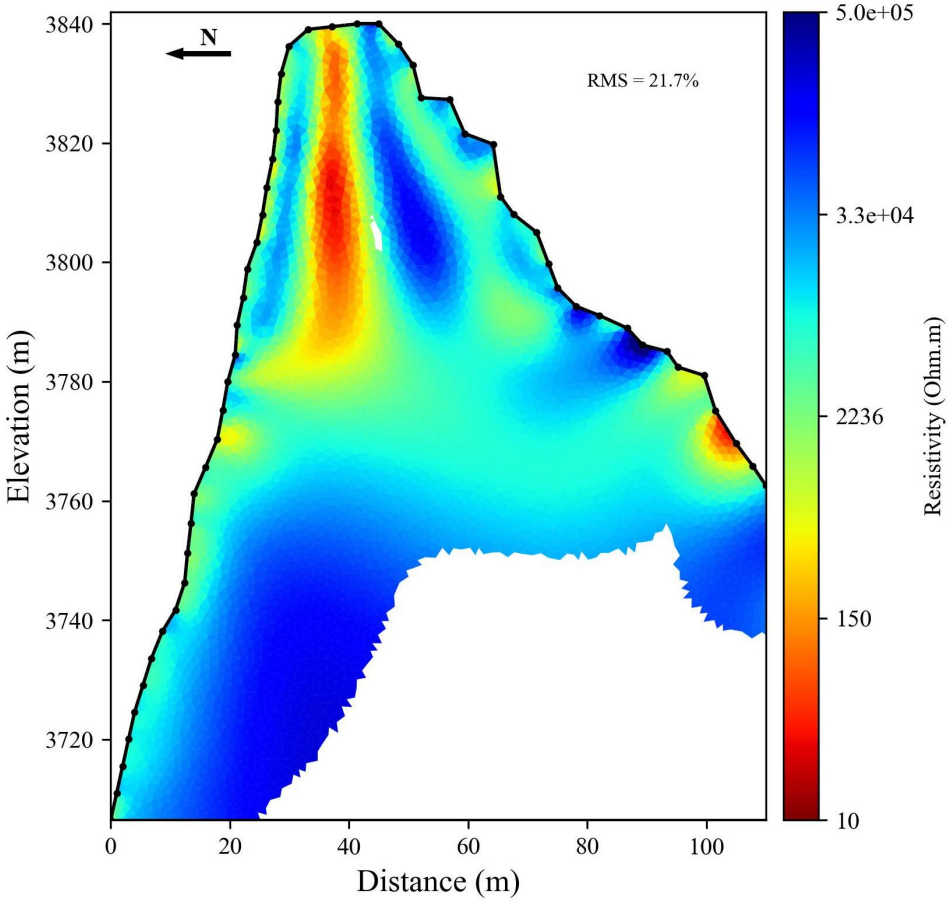

Figure 8. Electrical resistivity tomogram over the profile NW+E at the end of summer (September 25, 2021). Data acquisition on the East profile run into problems related to electrodes contact and cable malfunction. The last 10 electrodes from the E profile were removed during processing due to connection issues.

5.3. Time-lapse inversion

https://doi.org/10.5194/egusphere-2025-637
Preprint. Discussion started: 4 March 2025

To track the resistivity changes associated with nonlinear heat transfer such as heat advection across the site, a time-lapse inversion approach was employed. The reference model was moved along with the inversion so that the difference to the preceding step is constrained. Figure 9 shows the results of the time-lapse inversion of datasets from NW profile at different time intervals. Spatial and temporal changes in resistivity could be observed, while the anomaly related to the gallery (the warm-colored area (low resistivity area)) remains consistent over time. The permafrost identified by high resistivity, is observed in two zones, above and below the gallery. As expected, the most significant variations in resistivity occur near the surface in the active layer where thawing and freezing are visible through the steady resistivity changes. According to temperature analyzes conducted by Magnin et al. (2024), 2021 was cooler than both 2020 and 2022 (see Fig. 2). This is reflected in the tomograms by a more prominent cool-colored zone (more permafrost) in 2021 (Fig. 9e, f and g) in comparison with data in 2020 (Fig. 9c) and 2022 (Fig. 9l, taking into account the difference in dates). Furthermore, there is a significant variation in 2022 in the lower part of the tomograms (Fig. 9l), possibly related to water infiltration in fractures that shortcut the heat transfer from the surface to depth (Hasler et al., 2011). No evidence of water accumulation was observed from the geophysical measurements. It is suggested that the water table lies at lower altitude (Magnin and Josnin, 2021). However, this area is uncertain as it is located at the edge of the tomogram where sensitivity is low. In addition, the RMS error is high in these tomograms, indicating high uncertainties. Therefore, this information should be carefully considered and verified with further measurements focused on the zone of interest.

Instead of analyzing temporal resistivity changes in absolute terms, Figure 10 illustrates the resistivity variation ratio between two subsequent measurements. This approach facilitates the tracking and visualization of small changes in resistivity. A value of 1 (represented in white color) corresponds to no change in resistivity between the two measurements (reflecting

https://doi.org/10.5194/egusphere-2025-637
Preprint. Discussion started: 4 March 2025

consistent geological conditions, topographic effects, infrastructure or no considerable change in temperature over time), while the blue color indicates that the resistivity increased over time, and the red color represents the inverse. It can be observed that at short time interval (few days to weeks), the variation in resistivity is negligible (*e.g.*, Fig. 10b, e, f and j). At longer time interval (few weeks to months), only minor variations are noted (*e.g.*, Fig. 10a, h and i), while the seasonal variations are more pronounced as illustrated in Figure 10c, d and g. The effect of freezing is evident, marked by an increase in resistivity of the active layer (Fig. 10c and g). In contrast, Fig. 10d shows the maximum decrease in resistivity near the surface, as expected due to the thawing in the active layer. Further observations on Figures 10a, b and e indicate a local increase in resistivity, as shown by the blue color zone between 3780 and 3800 m a.s.l. That could be associated with water desaturation and drainage observed in the gallery just below this zone.

https://doi.org/10.5194/egusphere-2025-637
Preprint. Discussion started: 4 March 2025

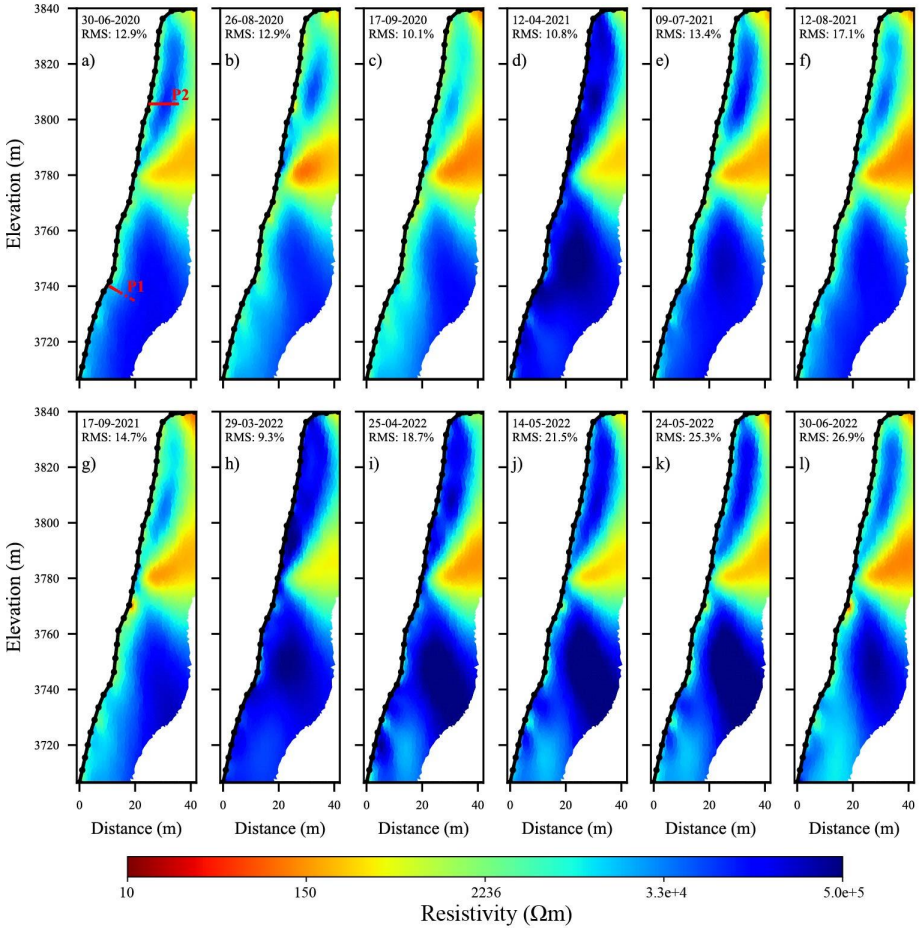

Figure 9. Electrical resistivity tomograms at different dates (from June-2020 to June-2022) along the NW side (NW profile). The conductive zone (in warm colors) denotes the presence of the gallery and elevator (see Fig. 1c). The red dots (P1 in panel a) indicate the positions of the thermal sensors in the borehole BH-NW. Data presented on Figures 13, 14 and 15 are extracted at the red dots (P1 and P2).

https://doi.org/10.5194/egusphere-2025-637
Preprint. Discussion started: 4 March 2025

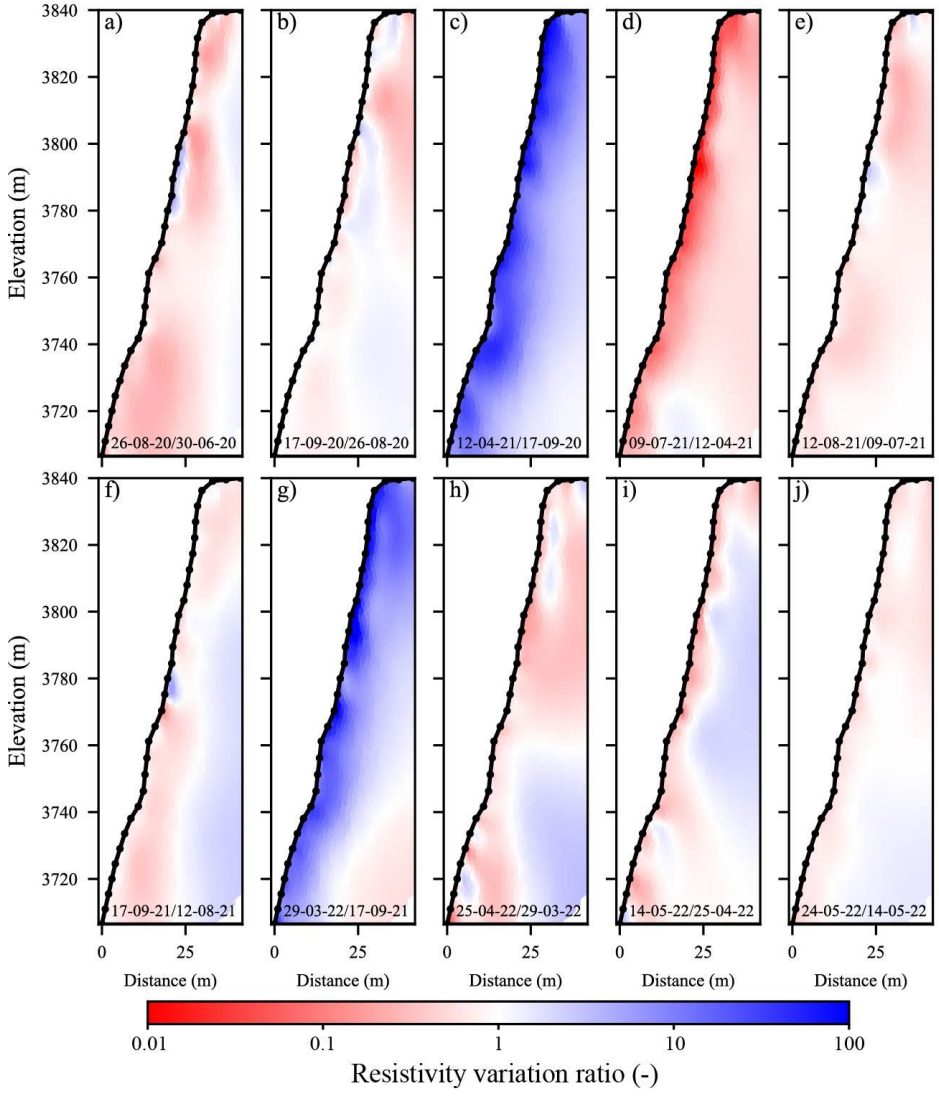

Figure 10. Resistivity variation ratio between consecutive electrical resistivity tomograms (shown in Fig. 9) along the NW side. Blue colors indicate an increase in resistivity, while red colors represent a decrease in resistivity from one measurement to the next.

On the south side, time-lapse inversion was also conducted using the same inversion parameters as those used on the NW side (Fig. 9). Figure 11 presents the results of the time-lapse inversion of datasets from S profile at various time intervals. Two phenomena can be

https://doi.org/10.5194/egusphere-2025-637
Preprint. Discussion started: 4 March 2025

distinguished on this side: first, in the lower part (*i.e.*, below the gallery denoted by the warm-colored area), seasonal variations in permafrost are clearly observed and could be tracked over time. In Figures 11a, c, d, g, h and l (measurements taken in summer and autumn), the steady thawing of active layer through heat conduction from the surface is evident in the lower part. Second, in the upper part of the profile (*i.e.*, above the gallery), the seasonal variations are less pronounced in this fractured area. This region is characterized by strong insolation (*i.e.*, sun-exposed area) that dries the rock and fractures, where drainage of water (of melted ice) reduces water saturation, thereby increasing resistivity near the surface as a result of air-filled pores and fractures. The water infiltration and drainage in this area increase the thickness of the active layer (*e.g.*, Figure 11a, d, g and h), and create a conductive zone observed beneath the fractured area where drainage is minimal or nonexistent (*e.g.*, Fig 11a, c, d and h).

Figure 12 illustrates the resistivity variation ratio between successive measurements on the S profile. The dynamics of the active layer are evident, with freezing-thawing effects visible near the surface (*e.g.*, Fig. 12a, d, and g). The heat effect (*i.e.*, decrease in resistivity values near the surface) is more pronounced in the lower section (below the gallery). Another type of anomaly could be observed at greater depth, where heat and/or cool waves resulting of heat transfer (with delay) lead to local variations at greater depth (*e.g.*, Fig. 12d, e, g and i). In contrast, the fractured zone in the upper portion obscures the temperature dependency of resistivity due to fluctuations in air and water content (*i.e.*, resistivity in this zone is impacted by factors beyond just temperature). Water infiltration in this area could explain the rapid and significant decrease in resistivity observed between 3790 and 3820 m a.s.l. (*e.g.*, Fig. 12c, f, and j), which increases the thickness of active layer in this zone.

https://doi.org/10.5194/egusphere-2025-637
Preprint. Discussion started: 4 March 2025

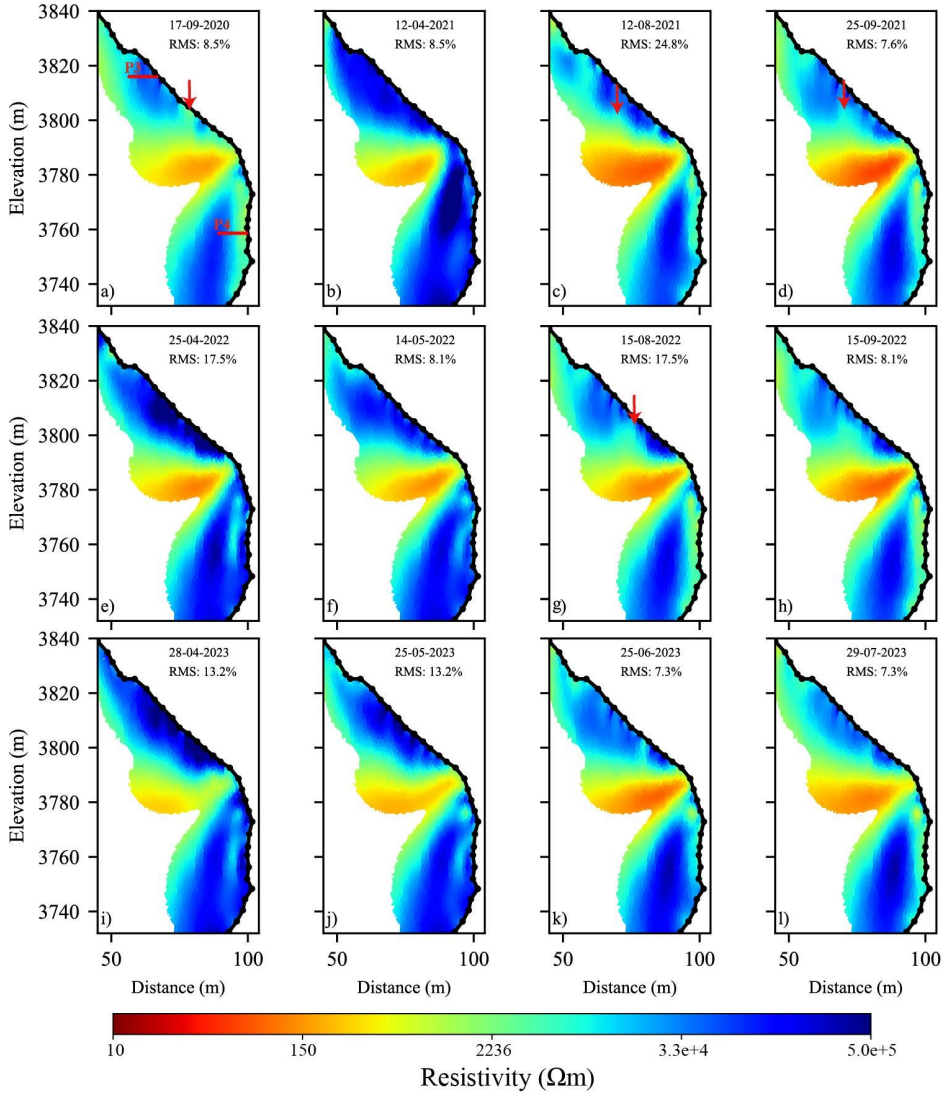

Figure 11. Electrical resistivity tomograms at different dates (from September-2020 to July-2023) along the South side (S profile). The conductive zone (in warm-colors) explained by the presence of the gallery (see Fig. 1d). Red arrows show the positions of possible infiltration or drainage. Data presented on Figure 13 are extracted at the red dots (P3 and P4) in panel a.

https://doi.org/10.5194/egusphere-2025-637
Preprint. Discussion started: 4 March 2025

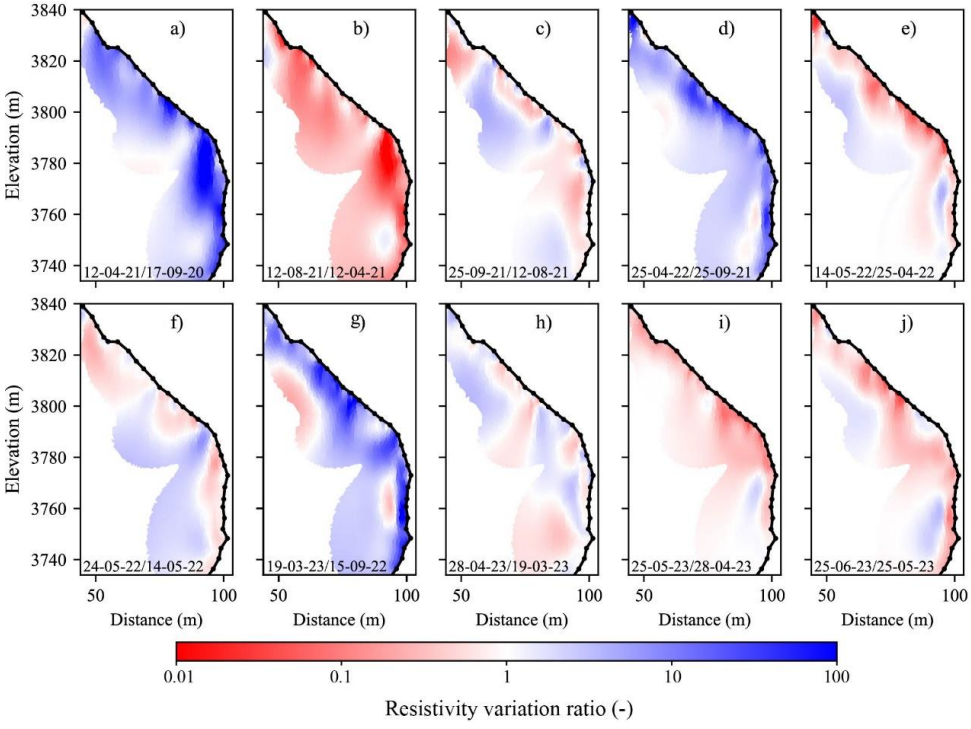

Figure 12. Resistivity variation ratio between consecutive electrical resistivity tomograms (shown in Fig. 11) along the South side. Blue colors indicate an increase in resistivity, while red colors represent a decrease in resistivity from one measurement to the next.

6. Discussion

In this study, we utilize A-ERT to investigate the evolution of permafrost at a high mountain site. We take advantage of the existing temperature borehole (BH-NW) located on the NW face along the geophysical profile (NW profile) to validate our interpretation and temperature estimations. For further analyses, inverted resistivity values are extracted at the borehole location (P1) for all temperature sensor depths up to 10 m (see Fig. 9), as well as at three other locations (P2, P3 and P4) illustrated in Figures 9 and 11.

https://doi.org/10.5194/egusphere-2025-637
Preprint. Discussion started: 4 March 2025

6.1. Permafrost dynamics from seasonal to pluri-annual time scale

The dynamics of the Active Layer (AL) are generally illustrated by the seasonal variations shown in Figures 9 and 11. The tomograms show the overall trend and the distribution of active layer and permafrost in the area. Data extracted at different locations, above and below the gallery (P1, P2 in Fig. 9 and P3, P4 in Fig. 11), are presented in Figure 13. These extracted resistivities reveal that the active layer is thicker in the upper section compared to the lower part, and that resistivity decreases over time in the permafrost.

On the NW side (P1 and P2), the variation of resistivity with depth is more pronounced at P2, which indicates a thicker AL compared to P1. The greater thickness of AL in the upper section can be explained by the 3D heat transfer and the proximity of the shaded face (NW side) to the sun-exposed faces (S side) in the top part (Noetzli et al., 2007). In the lower section at NW side (P1 in Fig. 13), the contrast between the resistivity in the active layer and that in the permafrost (frozen zone) is not significant, which may be due to low ice content where the porosity is around 1 %, or due to high surface conductivity in granite. The alteration of granite involves the transformation of primary minerals (mica and alkali feldspars) into secondary clay minerals (such as kaolinite), which are known for their high cation exchange capacity and, consequently, their contribution to surface conductivity (Piolat et al., 2025; Revil et al., 2024). However, it is important to note that the smallest quadrupole spacing is 15 m, which is insufficient to capture thin variations close to surface (Binley and Kemna, 2005).

On the South side (the sun-exposed face), above the gallery lies the fractured zone. The extracted resistivities at P3 (Fig. 13) reveal higher values compared to the NW side (P2), showing a difference of more than one orders of magnitude at the same altitude and time. The resistivity along P3 decreases slightly with depth, indicating that almost the entirety of P3 is within the active layer. In this zone, the active layer is thicker due to the fractures, which facilitate the heat transfer and water flow. Below the gallery at P4 (Fig. 13), the active layer is

https://doi.org/10.5194/egusphere-2025-637
Preprint. Discussion started: 4 March 2025

more distinct compared to P1 on the NW side, displaying more pronounced variations in resistivity with depth. Below the gallery on both sides, we observe that resistivity decreased over time at greater depths (*e.g.*, at P1, comparing data from July 30, 2020 and July 30, 2022, and at P4, comparing data from April 12, 2021 and April 28, 2023), indicating degradation of the permafrost. However, this decrease in resistivity is minor because the observation period is short.

Furthermore, in 2021, resistivity values were higher in both the upper and lower parts compared to 2020 and 2022, and this is aligned with temperature measurements (see Fig. 2) (see details in Magnin et al. (2024)). This indicate that A-ERT is able to reveal consistent permafrost evolution.

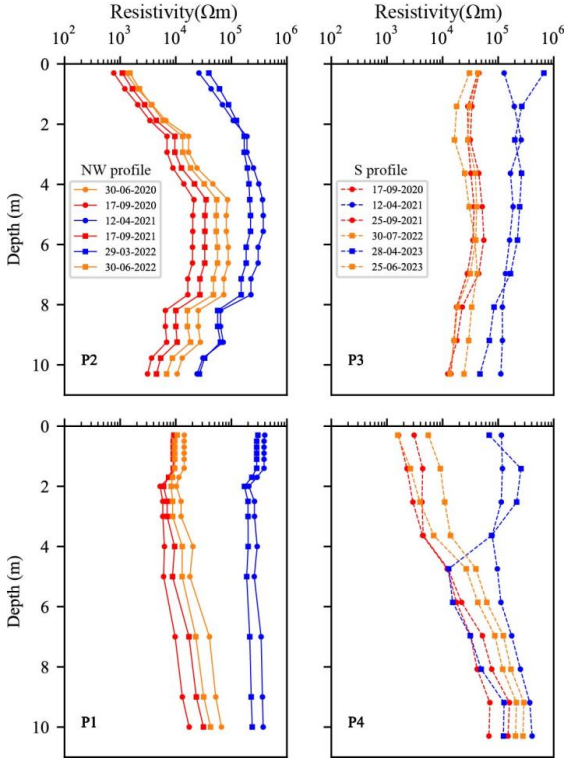

Figure 13. Resistivity extracted over depths at different locations. Resistivity extracted from tomograms on Figure 9 at P1 and P2, and from tomograms on Figure 11 at P3 and P4.

https://doi.org/10.5194/egusphere-2025-637
Preprint. Discussion started: 4 March 2025

6.2.Temperature - resistivity relationship

Extracted resistivity at P1 is superimposed at borehole BH-NW, where temperature measurements are available. We use these two datasets (*i.e.*, temperature and resistivity measurements at the same location, BH-NW) to explore the potential for estimating temperature based on the electrical resistivity measurements.

It is known that, when temperature > 0 °C (*i.e.*, the case in the active layer), resistivity depends on multiple variables, including porosity, water content, water salinity, Cation Exchange Capacity (CEC) and temperature (Revil et al., 2018) and will be difficult to model or to predict the resistivity value at this stage. In contrast, under frozen conditions, resistivity is assumed to be primarily dependent on temperature, while the other parameters remain constant. Therefore, the extracted resistivity was converted to temperature using the petrophysical model in Equation 2 (Duvillard et al., 2021; 2018; Coperey et al., 2019) in the frozen zone. Figure 14 shows the measured temperature alongside the estimated temperature from ERT data, plotted against depth at different dates (in summer and autumn). A good agreement can be observed between the measured and estimated temperature in frozen conditions, with differences of less than 1 °C at depths between 4 and 10 m. The data collected under frozen condition at the surface (*i.e.*, measured in winter and spring with high contact resistance) resulted in large discrepancy between the estimated and measured temperature, and could not be used to estimate temperature.

The estimated temperature presented in Figures 14 indicate that the proposed model (Equation 2) can accurately reproduce the temperature. Here we used data extracted after time-lapse inversion, however, conducting individual inversion and adjusting the inversion parameters can enhance this estimation of temperature. This suggests that temperature distribution across the site can be evaluated using this model (*e.g.*, Duvillard et al., 2021), assuming the medium is homogenous and resistivity variations are solely attributed to

https://doi.org/10.5194/egusphere-2025-637
Preprint. Discussion started: 4 March 2025

556 temperature. However, at AdM, this condition is not satisfied due to the infrastructure, which
557 creates a conductive zone within the medium (see Figs. 7, 9 and 11).
558

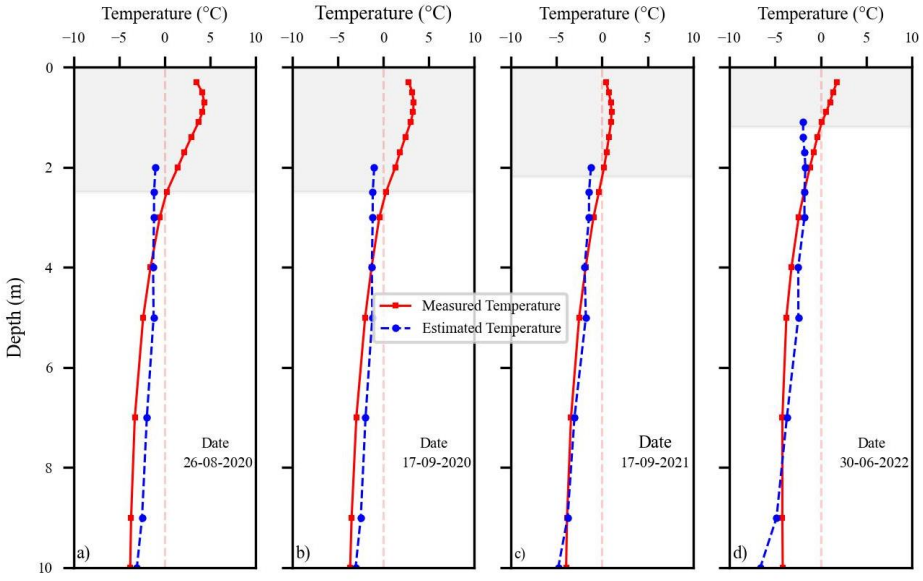

559

560 **Figure 14.** Comparison between measured temperatures in BH-NW and estimated temperatures from
561 geophysical measurements (*i.e.*, extracted resistivity values at different dates) using the petrophysical
562 model in Equation 2. The gray-shaded area marks the extent of the active layer at the time of
563 measurement. There is good agreement between measured and estimated temperature, with differences
564 of less than 1 °C at depths 4 to 10m. In the active layer, predicting temperature is not feasible since
565 temperature is not dominant factor affecting resistivity.
566

567 To go further in our analysis, Figure 15 shows the extracted resistivity at P1 vs.
568 temperature data measured in BH-NW at different dates. Laboratory measurements on both
569 granite samples (labeled Sample AdM and Sample Cosmiques) are also shown. Two key
570 observations can be made: first, data measured in winter and spring (frozen conditions at
571 surface) indicated by blue symbols, resistivity values are higher than what would be expected
572 based on the laboratory measurements, in agreement with the field observations in Maierhofer
573 et al (2024).

https://doi.org/10.5194/egusphere-2025-637
Preprint. Discussion started: 4 March 2025

Second, at higher temperature (*i.e.*, unfrozen conditions at surface), a linear trend is observed aligning with laboratory measurements for part of datasets. The difference of resistivity between field data and laboratory data in unfrozen conditions may be attributed to difference in water content and water salinity between field and laboratory conditions. The laboratory measurements were conducted in saturated conditions (saturation was performed under vacuum using degassed water). The freezing point, which is expected to result in a significant change in resistivity (as observed in laboratory measurements), does not exhibit the same effect in field. Actually, the transition between frozen and unfrozen conditions is not clearly distinguished in field. However, some datasets show gradual increase in resistivity when temperature decreased. Therefore, we hypothesize that the freezing occurs gradually at temperatures ranging between -0.5 and -2.5 °C. This point needs to be addressed in further research with smaller dispositive to improve the resolution of geophysical measurements.

This lack of clarity, observed between field data and laboratory data, may be attributed to several factors, including 3D effects at the site, the influence of infrastructure and heterogeneity at different scales (from fractures scale to pore scale where varying pore sizes led to variable residual water content available for electrical conduction). In addition, there is a difference in resolution between the two measurements: temperature measurements are local, while resistivity measurements account for a larger volume.

https://doi.org/10.5194/egusphere-2025-637
Preprint. Discussion started: 4 March 2025

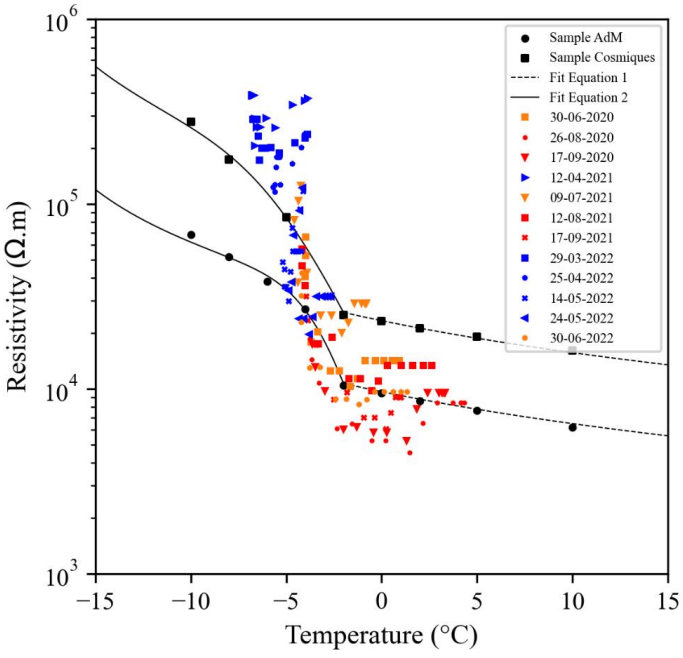

Figure 15. Resistivity *vs.* temperature. Resistivity is extracted from the tomograms in Figure 9 at location P1. Temperature is measured by sensors at BH-NW. Laboratory data on two granite samples and fitting with Equation 1 and 2 are shown too.

6.3. Hydrogeological dynamics

One of the objectives of this study was to assess the hydrogeological dynamics. While we could not precisely identify the infiltration and drainage pathways or the water table (which may be at a lower altitude), we did observe several instances that could be classified as evidence of water flux. With the AdM setting, we can hypothesize that the saturated conditions are almost never reached. There is water circulation but no accumulation of water and/or pressure because the water table is likely lower (Magnin and Josnin, 2021). As mentioned earlier, to validate these observations concerning water infiltration (*e.g.*, Fig. 9c, l), electrical resistivity measurements should be centered around the suspected zone at the base of the central peak of the AdM. On the other hand, on the south face, the tomograms show the near-surface desaturation of the pore-space attributed to the effect of the very strong insolation with a rock

https://doi.org/10.5194/egusphere-2025-637
Preprint. Discussion started: 4 March 2025

face that is perpendicular to the sun beam, and evidence of water infiltration along fractures (*e.g.*, Fig. 11e, f and i). The exact pathways of infiltration and drainage are still ambiguous, possibly due to the resolution of resistivity measurements. A-ERT acquisition using shorter spacing between electrodes improves the resolution near the surface, and could provide more detailed information about the subsurface.

7. Conclusions

We used an Automated Electrical Resistivity Tomography (A-ERT) to monitor permafrost dynamics over four years at AdM in the French Alps, in order to better understand the complexities of permafrost behavior in response to climatic variations. We summarize the key findings as follow:

- We highlight the critical influence of temperature on resistivity, revealing that the temperature-dependency of resistivity in field conditions is less pronounced than in controlled laboratory settings. This discrepancy could be attributed to the field's inherent heterogeneity (fractures network, infrastructures), a 3D site effect and the varying ice and water content within the rock which complicates the resistivity-temperature relationship. The results underscore the utility of ERT as a promising, non-invasive approach for monitoring permafrost evolution in high mountains, enabling the identification of permafrost
- Through detailed analyses of ERT data, we were able to characterize the active layer and identify significant seasonal and multiannual changes in permafrost dynamics. Importantly, we observed that the ALT varied significantly from one face to another in coherence with climate signal and measured temperatures in boreholes.
- This research demonstrate that temperature can be accurately derived from geophysical measurements of electrical resistivity based on a petrophysical model

https://doi.org/10.5194/egusphere-2025-637
Preprint. Discussion started: 4 March 2025

connecting resistivity to temperature with precision of ±1 °C at depths between 4 and 10 m.

- Our assessments of the hydrogeological system revealed instances of water flux; however, the exact pathways of infiltration and drainage remain unclear.
- Additionally, the study highlights the urgent need to address challenges related to climate conditions at high-altitudes that affect device performance and contact resistances, in order to improve the reliability of continuous A-ERT data collection.

Future research should focus on refining the methods for better resolving subsurface properties, particularly in areas with complex hydrological dynamics. Incorporating induced polarization measurements could enhance the interpretation of resistivity data concerning of water and ice contents.

Data availability. Data will be made available on request.

Author contributions. FA performed the data analysis, prepared the figures, and wrote the majority of the text. JB contributed to data acquisition, writing, and figure preparation. FM and AR contributed to the design of the ERT survey, as well as data acquisition and discussion of the results. EM, MBA and PAD contributed to the field installation and acquisition, JR conducted and processed the laboratory data, MK contributed to data inversion and discussion, TC provided air temperature data, LR and PD offered additional information about the site. Finally, all authors actively contributed to the preparation of this version of the paper.

Competing interests. The authors declare that they have no conflict of interest.

Acknowledgments. This research is part of the ANR WISPER project (ANR-19-CE01-0018) and the Action Plan on Risks from Glacial and Periglacial Origin (PAPROG) from the French

https://doi.org/10.5194/egusphere-2025-637
Preprint. Discussion started: 4 March 2025

Ministry of Ecological Transition, Biodiversity, Forest, Sea and Fishing. The authors acknowledge the numerous people that helped with the field work: Antoine Chabas, Bruno Galabertier and Raphaël Gallet from the EDYTEM Laboratory, Simon Alesina from the University of Lausanne, Marc Cleriot for help with field work, and Catherine Coulaud from IGE. The authors are also grateful towards the Compagnie du Mont-Blanc that provided access to the site and support.

https://doi.org/10.5194/egusphere-2025-637
Preprint. Discussion started: 4 March 2025

References

Abdulsamad, F., Revil, A., Ghorbani,A., Toy, V., Kirilova, M., Coperey, A., Duvillard, P. A., Ménard, G., and Ravanel, L. Complex conductivity of graphitic schists and sandstones. Journal of Geophysical Research: Solid Earth, 124, 8223‑8249. https://doi.org/10.1029/2019JB017628, 2019.

Binley, A. and Kemna, A.: DC Resistivity and Induced Polarization Methods, in: Hydrogeophysics, Water Science and Technology Library book series, edited by: Rubin, Y. and Hubbard, S. S.,volume 50, 129‑156, https://doi.org/10.1007/1-4020-3102-5_5, 2005.

Campbell, S., Rosa T. Affleck, Sinclair, S. Ground-penetrating radar studies of permafrost, periglacial, and near-surface geology at McMurdo Station, Antarctica. Cold Regions Science and Technology, 148, Pages 38-49, https://doi.org/10.1016/j.coldregions.2017.12.008, 2018.

Cathala, M., Bock, J., Abdulsamad, F., Deline, P., Josnin, J-Y., Ravanel, L., Revil, A., Richard, J., Verroust, F., and Magnin, F. Assessing the role of permafrost in the preconditioning and triggering factors of the September 2020 Crête des Grangettes rockfall (southern French Alps), Géomorphologie: relief, processus, environnement, 30, 3, 171-188, https://doi.org/10.4000/12yqn, 2024.

Coperey, A., Revil, A., Abdulsamad, F., Stutz, B., Duvillard, P.A., and Ravanel, L. Low frequency induced polarization of porous media undergoing freezing: preliminary observations and modeling, Journal of Geophysical Research: Solid Earth, 124, doi:10.1029/2018JB017015, 2019.

Dahlin, T., and Zhou, B. A numerical comparison of 2D resistivity imaging with 10 electrode arrays, Geophys. Prospect., 52, 379–398. https://doi.org/10.1111/j.1365-2478.2004.00423.x, 2004.

Doetsch, J., Ingeman-Nielsen, T., Christiansen, A. V., Fiandaca, G.,Auken, E., and Elberling, B.: Direct current (DC) resistivity and induced polarization (IP) monitoring of active layer dynamics at high temporal resolution, Cold Reg. Sci. Technol., 119, 16‑28, https://doi.org/10.1016/j.coldregions.2015.07.002, 2015.

Draebing, D. Application of refraction seismics in alpine permafrost studies: A review, Earth-Science Reviews, 155, 136–152, https://doi.org/10.1016/j.earscirev.2016.02.006, 2016.

https://doi.org/10.5194/egusphere-2025-637
Preprint. Discussion started: 4 March 2025

691 Duvillard, P. A., Revil, A., Qi, Y., Soueid Ahmed, A., Coperey, A., and Ravanel, L.: Three-Dimensional
692 Electrical Conductivity and Induced Polarization Tomography of a Rock Glacier, J. Geophys. Res.-
693 Sol. Ea., 123, 9528‐9554, https://doi.org/10.1029/2018JB015965, 2018.
694 Duvillard, P.A., Magnin, F., Revil, A., Legay, A., Ravanel, L., Abdulsamad, F., and Coperey, A.:
695 Temperature distribution in a permafrost-affected rock ridge from conductivity and induced
696 polarization tomography, Geophys. J. Int., 225, 1207‐1221, https://doi.org/10.1093/gji/ggaa597,
697 2021.
698 Etzelmüller, B., Guglielmin, M., Hauck, C., Hilbich, C., Hoelzle, M., Isaksen, K., Noetzli, J., Oliva, M.,
699 and Ramos, M.Twenty years of European mountain permafrost dynamics−the PACE legacy.
700 Environmental Research Letters, 15(10), 104070. Available from: https://doi.org/10.1088/1748-
701 9326/abae9d, 2020.
702 Farzamian M, Vieira G, Monteiro Santos FA, et al. Detailed detection of active layer freeze-thaw
703 dynamics using quasi-continuous electrical resistivity tomography (Deception Island, Antarctica).
704 Cryosphere.14(3):1105-1120. https://doi.org/10.5194/tc-14-1105-2020, 2020.
705 Günther, T., Rücker, C., and Spitzer, K. Three-dimensional modelling and inversion of dc resistivity
706 data incorporating topography-II. Inversion. Geophysical Journal International, Volume 166, Issue
707 2, August 2006, Pages 506–517, https://doi.org/10.1111/j.1365-246X.2006.03011.x, 2006.
708 Hasler, A., Gruber. S., Font. M., and Dubois. A. Advective Heat Transport in Frozen Rock Clefts:
709 Conceptual Model, Laboratory Experiments and Numerical Simulation, Permafrost and Periglacial
710 Processes, 22, 378–389, https://doi.org/10.1002/ppp.737, 2011.
711 Hauck, C., Böttcher, M., and Maurer, H.: A new model for estimating subsurface ice content based on
712 combined electrical and seismic data sets, The Cryosphere, 5, 453–468, https://doi.org/10.5194/tc-
713 5-453-2011, 2011.
714 Hauck, C., and Hilbich C. Preconditioning of mountain permafrost towards degradation detected by
715 electrical resistivity. Environ. Res. Lett. 19 064010. https://doi.org/10.1088/1748-9326/ad3c55,
716 2024.

https://doi.org/10.5194/egusphere-2025-637
Preprint. Discussion started: 4 March 2025

717 Herring T, Lewkowicz AG, Hauck C, et al. Best practices for using electrical resistivity tomography to
718 investigate permafrost. Permafrost and Periglac Process. 1-19. https://doi.org/10.1002/ppp.2207,
719 2023.
720 Hilbich, C., Marescot, L., Hauck, C., Loke, M. H., and Mäusbacher, R.: Applicability of Electrical
721 Resistivity Tomography Monitoring to Coarse Blocky and Ice-rich Permafrost Landforms,
722 Permafrost Periglac., 20, 269–284, https://doi.org/10.1002/ppp.652, 2009.
723 Hilbich, C., Hauck, C., Hoelzle, M., Scherler, M., Schudel, L., Völksch, I., Vonder Mühll, D., and
724 Mäusbacher, R. Monitoring Mountain permafrost evolution using electrical resistivity tomography:
725 A 7-year study of seasonal, annual, and long-term variations at Schilthorn, Swiss Alps, J. Geophys.
726 Res.-Earth, 113, F01S90, https://doi.org/10.1029/2007JF000799, 2008.
727 Jacquemart, M., Weber, S., Chiarle, M., Chmiel, M., Cicoira, A., Corona, C., Eckert, N., Gaume, J.,
728 Giacona, F., Hirschberg, J., Kaitna, R., Magnin, F., Mayer, S., Moos, C., van Herwijnen, A., and
729 Stoffel, M.: Detecting the impact of climate change on alpine mass movements in observational
730 records from the European Alps, Earth-Science Reviews, 258, 104886,
731 https://doi.org/10.1016/j.earscirev.2024.104886, 2024.
732 Karaoulis, M., Tsourlos, P., Kim, J., and Revil, A.: 4D time-lapse ERT inversion: introducing combined
733 time and space constraints, Near Surf. Geophys., 12, 25–34, https://doi.org/10.3997/1873-
734 0604.2013004, 2013.
735 Keuschnig, M., Krautblatter,M., Hartmeyer, I., Fuss, C. and Schrott, L. Automated electrical resistivity
736 tomography testing for early warning in unstable permafrost rock walls around Alpine
737 infrastructure, Permafrost Periglac. Process., 28, 158–171. https://doi.org/10.1002/ppp.1916, 2017.
738 Krautblatter, M. and Hauck, C.: Electrical resistivity tomography monitoring of permafrost in solid rock
739 walls, J. Geophys. Res., 112, F02S20, https://doi.org/10.1029/2006JF000546, 2007.
740 Krautblatter M, Verleysdonk S, Flores-Orozco A., and Kemna A. Temperature-calibrated imaging of
741 seasonal changes in permafrost rock walls by quantitative electrical resistivity tomography
742 (Zugspitze, German/Austrian Alps). J Geophys Res Earth. 115(2):1-15.
743 https://doi.org/10.1029/2008JF001209, 2010.

https://doi.org/10.5194/egusphere-2025-637
Preprint. Discussion started: 4 March 2025

744 Krautblatter, M., Funk, D. and G¨unzel, F.K. Why permafrost rocks become unstable: a rock–ice-
745 mechanical model in time and space. Earth Surf. Process. Landforms, 38, 876–887.
746 https://doi.org/10.1002/esp.3374, 2013.
747 Loke, M. H. Time-lapse resistivity imaging inversion, paper presented at 5th Meeting of the
748 Environmental and Engineering Society European Section, Budapest. 1999.
749 Magnin, F., Deline, P., Ravanel, L., Noetzli, J., and Pogliotti, P.: Thermal characteristics of permafrost
750 in the steep alpine rock walls of the Aiguille du Midi (Mont Blanc Massif, 3842 m a.s.l), The
751 Cryosphere, 9, 109–121, https://doi.org/10.5194/tc-9-109-2015, 2015b.
752 Magnin, F., Krautblatter, M., Deline, P., Ravanel, L., Malet, E. and Bevington, A. Determination of
753 warm, sensitive permafrost areas in near-vertical rockwalls and evaluation of distributed models by
754 electrical resistivity tomography, J. geophys. Res., 120, 745–762.
755 https://doi.org/10.1002/2014JF003351, 2015a.
756 Magnin, F., Ravanel, L., Bodin, X., Deline, P., Malet, E., Krysiecki, J.-M., et al. Main results of
757 permafrost monitoring in the French Alps through the PermaFrance network over the period 2010–
758 2022. Permafrost and Periglacial Processes, 35(1), 3–23. https://doi.org/10.1002/ppp.2209, 2024
759 Magnin, F. and Josnin, J.-Y. Water flows in Rock Wall permafrost: a numerical approach coupling
760 hydrological and thermal processes. Journal of Geophysical Research - Earth Surface, 126(11),
761 e2021JF006394. https://doi.org/10.1029/2021JF006394, 2021.
762 Maierhofer, T., Flores Orozco, A., Roser, N., Limbrock, J. K., Hilbich, C., Moser, C., Kemna, A., Drigo,
763 E., Morra di Cella, U., and Hauck, C.: Spectral induced polarization imaging to monitor seasonal
764 and annual dynamics of frozen ground at a mountain permafrost site in the Italian Alps, The
765 Cryosphere, 18, 3383–3414, https://doi.org/10.5194/tc-18-3383-2024, 2024.
766 Mewes, B., Hilbich, C., Delaloye, R., and Hauck, C.: Resolution capacity of geophysical monitoring
767 regarding permafrost degradation induced by hydrological processes, The Cryosphere, 11, 2957–
768 2974, https://doi.org/10.5194/tc-11-2957-2017, 2017.
769 Mollaret, C., Wagner, F. M., Hilbich, C., Scapozza, C., and Hauck, C.: Petrophysical Joint Inversion
770 Applied to Alpine Permafrost Field Sites to Image Subsurface Ice, Water, Air, and Rock Contents,
771 Front. Earth Sci., 8, 1–25, https://doi.org/10.3389/feart.2020.00085, 2020.

https://doi.org/10.5194/egusphere-2025-637
Preprint. Discussion started: 4 March 2025

772 Mollaret, C., Hilbich, C., Pellet, C., Flores-Orozco, A., Delaloye, R., and Hauck, C.: Mountain
773 permafrost degradation documented through a network of permanent electrical resistivity
774 tomography sites, The Cryosphere, 13, 2557–2578, https://doi.org/10.5194/tc-13-2557-2019, 2019.
775 Noetzli J., Gruber S., Kohl T., Salzmann N., Haeberli W. Three-dimensional distribution and evolution
776 of permafrost temperatures in idealized high-mountain topography. Journal of Geophysical
777 Research: Earth Surface 112, n/a–n/a. https://doi.org/10.1029/2006JF000545, 2007.
778 Moser, C., Morra di Cella, U., Hauck, C., and Flores Orozco, A.: Spectral induced polarization survey
779 for the estimation of hydrogeological parameters in an active rock glacier, The Cryosphere, 19,
780 143–171, https://doi.org/10.5194/tc-19-143-2025, 2025.
781 Offer, M., Weber, S., Krautblatter, M., Hartmeyer, I., and Keuschnig, M.: Pressurised water flow in
782 fractured permafrost rocks revealed by borehole temperature, electrical resistivity tomography, and
783 piezometric pressure, The Cryosphere, 19, 485–506, https://doi.org/10.5194/tc-19-485-2025, 2025.
784 Pavoni, M., Boaga, J., Wagner, F. M., Bast, A., Phillips, M. Characterization of rock glaciers
785 environments combining structurally-coupled and petrophysically-coupled joint inversions of
786 electrical resistivity and seismic refraction datasets, Journal of Applied Geophysics, 215, 0926-
787 9851, https://doi.org/10.1016/j.jappgeo.2023.105097, 2023.
788 Piolat, L., Revil, A., Richard, J., Ghorbani G., Cosme, P., Géraud, Y., Casotti, C., Vaudelet, P., Diraison,
789 M., and Favier, A., 2025.Induced polarization of volcanic rocks. 8. The case of intrusive igneous
790 rocks. Submitted, Geophysical Journal International
791 Ravanel, L., Magnin, F. and Deline, P. Impacts of the 2003 and 2015 summer heatwaves on permafrost-
792 affected rock-walls in the Mont Blanc massif. Science of the Total Environment, 609, 132–143.
793 https://doi.org/10.1016/j.scitotenv.2017.07.055, 2017.
794 Revil, A., Cathles, L. M., Losh, S., & Nunn, J. A. Electrical conductivity in shaly sands with geophysical
795 applications. Journal of Geophysical Research, 103(B10), 23,925–23,936.
796 https://doi.org/10.1029/98JB02125, 1998.
797 Revil, A., Ghorbani, A., Zhao, X., Mouyeaux, A., Barrère, L., Richard, J., Peyras, L., and Vaudelet, P.
798 Groundwater flow paths using combined self-potential, electrical resistivity, and induced

https://doi.org/10.5194/egusphere-2025-637
Preprint. Discussion started: 4 March 2025

polarization signals, Geophysical Journal International, 239, 2, 798–820, https://doi.org/10.1093/gji/ggae291, 2024.

Revil, A., Coperey, A., Mao, D., Abdulsamad, F., Ghorbani, A., Rossi, M., and Gasquet, D,. Induced polarization response of porous media with metallic particles — Part 8: Influence of temperature and salinity: Geophysics, 83, no. 6, E435–E456, https://doi.org/10.1190/geo2018-0089.1, 2018.

Rücker, C., Günther, T., and Wagner, F. M.: pyGIMLi: An open-source library for modelling and inversion in geophysics, Computers & Geosciences, 109, 106–123, https://doi.org/10.1016/j.cageo.2017.07.011, 2017.

Scandroglio R, Draebing D, Offer M, Krautblatter M. 4D quantification of alpine permafrost degradation in steep rock walls using a laboratory-calibrated electrical resistivity tomography approach. Near Surface Geophys.19(2):241-260. https://doi.org/10.1002/nsg.12149, 2021.

Steiner, M., Wagner, F. M., and Flores Orozco, A.: Improved characterization of alpine permafrost through structurally constrained inversion of refraction seismic data, The Cryosphere Discuss, https://doi.org/10.5194/tc-2019-52, 2019.

Steiner, M., Wagner, F. M., Maierhofer, T., Schöner, W., and Flores Orozco, A. Improved estimation of ice and water contents in alpine permafrost through constrained petrophysical joint inversion: The Hoher Sonnblick case study," GEOPHYSICS 86: WB61-WB75. https://doi.org/10.1190/geo2020-0592.1, 2021.

Wagner, F. M., Mollaret, C., Kemna, A., and Hauck, C.: Quantitative imaging of water, ice and air in permafrost systems through petrophysical joint inversion of seismic refraction and electrical resistivity data, Geophys. J. Int., 219, 1866–1875, https://doi.org/10.1093/gji/ggz402, 2019.

Zimmermann, E., Kemna, A., Berwix, J., Glaas, W., Münch, H. M., and Huisman, J. A. A high accuracy impedance spectrometer for measuring sediments with low polarizability. Measurement Science and Technology, 19(10), 105603. https://doi.org/10.1088/0957-0233/19/10/105603, 2008.